

# Deep Diversity-Enhanced Feature Representation of Hyperspectral Images

Jinhui Hou, Zhiyu Zhu, Junhui Hou, Hui Liu, Huanqiang Zeng, and Deyu Meng

**Abstract**—In this paper, we study the problem of embedding the high-dimensional spatio-spectral information of hyperspectral (HS) images efficiently and effectively, oriented by feature diversity. To be specific, based on the theoretical formulation that feature diversity is correlated with the rank of the unfolded kernel matrix, we rectify 3D convolution by modifying its topology to boost the rank upper-bound, yielding a rank-enhanced spatial-spectral symmetrical convolution set (ReS<sup>3</sup>-ConvSet), which is able to not only learn diverse and powerful feature representations but also save network parameters. In addition, we also propose a novel diversity-aware regularization (DA-Reg) term, which acts directly on the feature maps to maximize the independence among elements. To demonstrate the superiority of the proposed ReS<sup>3</sup>-ConvSet and DA-Reg, we apply them to various HS image processing and analysis tasks, including denoising, spatial super-resolution, and classification. Extensive experiments demonstrate that the proposed approaches outperform state-of-the-art methods to a significant extent both quantitatively and qualitatively. The code is publicly available at <https://github.com/jinhui/ReSSS-ConvSet>.

**Index Terms**—Hyperspectral imagery, deep learning, feature diversity, feature extraction, denoising, classification, super-resolution.

## 1 INTRODUCTION

THE rich spectral information of hyperspectral (HS) images towards real-world scenes/objects has facilitated applications in numerous fields, such as military [1], agriculture [2], and marine monitoring [3]. In recent years, owing to the powerful representational ability, a considerable number of deep learning-based methods for HS image processing and analysis have been proposed, where one fundamental and crucial issue is *how to embed the high-dimensional spatial-spectral information of HS images effectively and efficiently*. Generally, most of existing works extract spatial-spectral features of HS images by applying 2-D conventional filters with multiple channels on each cube slice separately [4], [5], [6], 3-D conventional filters to simultaneously convolve in spatial and spectral domains [7], [8], [9], or a 2-D and 3-D conventional filters combined network [10], [11]. However, these empirically designed feature extraction/embedding modules are hard to provide quantitative instructions for network designing and may be not optimal, thus limiting performance. Besides, most of them tend to stack off-the-shelf modules to build complicated and large-capacity networks for pursuing high performance, such as multi-scale strategy [8], [10], [12], [13], [14], attention mechanism [13], [15], [16], and atrous convolution [13], [17].

Unlike existing works, we tackle this fundamental prob-

lem from the perspective of enhancing feature diversity that has demonstrated the importance to the performance of downstream applications [18], [19]. Specifically, starting from 3D convolution, the intuitive choice for modeling HS images, we theoretically quantify the diversity of features with the rank of the 2-D matrix, enabling us to boil the problem of learning diverse spatio-spectral representations down to boosting the upper bound of the rank of the matrix formed by the convolution kernels. We then ingeniously modify the network topology, naturally yielding our rank-enhanced spatial-spectral symmetrical convolution set (ReS<sup>3</sup>-ConvSet) which is able to learn diverse spatial-spectral features and further save network parameters. Besides, we also propose a novel diversity-aware regularization (DA-Reg) term, which directly optimizes the distribution of the singular values of the 2-D matrix formed by features for promoting diversity. Finally, based on the proposed ReS<sup>3</sup>-ConvSet and DA-Reg, we construct three learning-based frameworks for HS image denoising, spatial super-resolution, and classification to demonstrate their significance. Extensive experiments on commonly used HS image benchmark datasets demonstrate the significant superiority of the proposed methods over state-of-the-art ones.

In summary, the main contributions of this paper are four-fold:

- J. Hou, Z. Zhu, and J. Hou are with the Department of Computer Science, City University of Hong Kong, Hong Kong (e-mail: jhhou3-c@my.cityu.edu.hk; zhiyuzhu2@my.cityu.edu.hk; jh.hou@cityu.edu.hk).
- H. Liu is with the School of Computing & Information Sciences, Caritas Institute of Higher Education, Hong Kong. (e-mail: hliu99-c@my.cityu.edu.hk).
- H. Zeng is with the School of Information Science and Engineering, Huaqiao University, Xiamen, China (e-mail: zeng0043@hqu.edu.cn).
- D. Meng is with the School of Mathematics and Statistics, Xi'an Jiaotong University, Xi'an 710049, China (e-mail: dymeng@mail.xjtu.edu.cn).
- The first two authors contributed to this paper equally. This work was supported by the Hong Kong Research Grants Council under Grants 11219019 and 11218121. Corresponding author: Junhui Hou.
- an efficient and effective spatial-spectral feature representation module based on theoretical analysis;
- a simple yet effective loss promoting feature diversity;
- comprehensive and quantitative investigations on various convolution manners for HS images;
- new learning-based methods for HS image processing, including HS image denoising, spatial super-resolution, and classification, producing state-of-the-art performance.
- revealing the importance of feature extraction, which

may shed light on deep learning-based HS image processing and analysis.

The remainder of the paper is organized as follows. Section 2 reviews the existing related works, including HS image denoising, HS image spatial super-resolution, and HS image classification. Section 3 describes our proposed ReS<sup>3</sup>-ConvSet in detail, which is further incorporated into various HS image processing tasks in Section 4, including HS image denoising, spatial super-resolution, and classification. In Section 5, we conduct extensive experiments and comparisons to demonstrate the advantages of the proposed methods, as well as comprehensive ablation studies. Finally, Section 6 concludes this paper.

## 2 RELATED WORK

In this section, we briefly review deep learning-based methods for HS image processing and analysis, including HS image denoising, spatial super-resolution, and classification. We also refer readers to [20], [21], [22] for the comprehensive survey on these topics.

### 2.1 HS Image Denoising

Recently, a considerable number of deep learning-based methods for HS image denoising have been presented, which improve the restoration quality of traditional optimization-based methods dramatically. For example, Chang *et al.* [4] first tackled HS image denoising by a deep neural network, in which the learned 2-D filters with multiple channels were utilized. Yuan *et al.* [10] designed a novel spatial-spectral network with both 2-D and 3-D convolutional kernels to fully exploit spatial and spectral features. Liu *et al.* [17] presented a 3-D atrous denoising convolution neural network by integrating the atrous convolution operation to enlarge the receptive fields in the spatial and spectral dimensions simultaneously. Inspired by the separable 3-D spatial-temporal convolution [23], Dong *et al.* [24] proposed a separable 3-D convolution network to explore spatial-spectral correlations by decomposing 3-D convolution into the concatenation of 2-D spatial convolution and 1-D spectral convolution. Wei *et al.* [25] proposed a 3-D quasi-recurrent neural network (QRNN3D) to simultaneously explore the structural spatio-spectral correlation and global correlation along spectral. Besides, an alternating directional structure was integrated to alleviate the spatio-spectral dependence modeling. Zhang *et al.* [26] constructed a framework by combining the low-rank physical property into a deep convolutional neural network. Shi *et al.* [13] designed a 3-D attention denoising network with two parallel branches, including spatial branch with the position attention module and spectral branch with the channel attention module. Cao *et al.* [6] designed a deep spatial-spectral global reasoning network (GRN) to explore the contextual information by combining the local and global spatial-spectral information of HS images. Rui *et al.* [27] presented a data-driven method to capture the general weighting principle of HS image denoising model. Bodrito *et al.* [28] proposed a trainable spectral-spatial sparse coding (T3SC) model by employing sparse coding and deep learning.

### 2.2 HS Image Spatial Super-resolution

In recent years, many HS image spatial super-resolution methods [5], [7], [11], [29], [30], [31], [32], [33], [34], [35] has been proposed by introducing deep learning techniques in this task, leading to a significant process. Yuan *et al.* [29] proposed a transfer learning framework for recovering high-spatial-resolution HS images via propagating the knowledge from nature images. Mei *et al.* [7] designed a 3-D full convolution neural network (3DFCNN) to explore the spatial context in adjacent areas and the spectral correlation in adjacent bands simultaneously. Jiang *et al.* [5] proposed a spatial-spectral prior framework, called SSPSR, equipped with grouped convolutions and progressive upsampling strategies. Li *et al.* [30] introduced a generative adversarial network into HS image super-resolution, in which 3-D CNN and band attention mechanism were adopted. Wang *et al.* [11] designed a dual-channel network, where 2-D and 3-D CNN were combined to jointly learn spectrum and feature context. Hu *et al.* [31] proposed an intrafusion network with spectral difference, parallel convolution, and intrafusion modules. In [32], the relationship between 2-D and 3-D convolution was explored for enhancing HS image super-resolution. Li *et al.* [33] proposed a novel multi-task learning network to jointly tackle the main task (i.e., HS image super-resolution) and the auxiliary task (i.e., RGB image super-resolution). Wang *et al.* [34] presented a recurrent feedback network for capturing the consecutive information among spectral bands via modeling the HS bands in the sequential way. Hou *et al.* [35] designed a novel deep posterior distribution-based embedding framework with a set of carefully-defined HS embedding events to extract the high-dimensional spatial-spectral information from the probabilistic perspective.

### 2.3 HS Image Classification

The early works tackle HS image classification by applying conventional machine learning methods, such as support vector machines (SVMs) [36], random forest (RF) [37], Gaussian process [38], K-nearest neighbors (KNNs) [39], linear discriminant analysis [40], and principal component analysis (PCA) [41]. Owing to limited representation capability, these methods are insufficient to handle the complex spatial-spectral information of HS images. Benefiting from the rapid development of deep learning techniques, many deep learning-based methods for HS image classification have been proposed. Primarily, a considerable number of advanced networks, e.g., stacked autoencoders (SAEs) [42], convolutional neural networks (CNNs) [9], [43], [44], [45], recurrent neural networks (RNNs) [46], graph convolutional networks (GCNs) [47], generative adversarial networks (GANs) [48], Transformer [49], were employed to improve the HS image classification accuracy. To be specific, Hu *et al.* [43] adopted 1-D CNN. Chen *et al.* [44] and Hamida *et al.* [9] applied 3-D CNN to extract the spectral-spatial features of HS images. Paoletti *et al.* [45] proposed a deep pyramidal residual network to obtain accurate HS image classification utilizing spectral and spatial information. Mou *et al.* [46] presented a novel RNN model for HS image classification by regarding the HS pixels as sequential data. Hong *et al.* [47] introduced a minibatch GCN and investigated CNN

and GCN with different fusion approaches. Hang *et al.* [48] designed a multi-task GAN by undertaking reconstruction and classification tasks. Hong *et al.* [49] proposed a new backbone network based on transformer, named SpectralFormer, focusing on extracting spectral information of HS images. In addition, many deep learning strategies, e.g., multi-scale [12], [14], attention mechanism [15], [16], were adopted for pursuing high classification performance. Wan *et al.* [14] proposed a unified multi-scale learning framework equipped with a multi-scale spatial-channel attention mechanism and a multi-scale shuffle block. Paoletti *et al.* [16] presented a novel multiple attention-guided capsule network for HS image classification.

### 3 PROPOSED METHOD

Despite the HS image contains rich information that facilitates subsequent applications, its high-dimensional characteristic enables various possibilities of the feature representation process, thus posing challenges in determining the optimal one. Previous studies [50], [51] show that improving feature diversity is one of the most promising solutions to overcome network redundancy, thus fully utilizing the model capacity. Thus, we tackle such a fundamental issue from the perspective of promoting the diversity of features via quantitative modeling, which further guides us to design the efficient yet powerful feature embedding module.

#### 3.1 Quantitative Modeling of Feature Diversity

Let  $\mathcal{A} \in \mathbb{R}^{M \times C \times k \times k \times k}$  be the kernel tensor of a typical 3-D convolutional layer with  $M$  3-D kernels of size  $k \times k \times k$ , where  $C$  is the number of input feature channels. By feeding an HS feature map  $\mathcal{I} \in \mathbb{R}^{C \times B \times H \times W}$ , the 3-D convolutional layer outputs feature map  $\mathcal{F} \in \mathbb{R}^{M \times B' \times H' \times W'}$ . We can equivalently express the 3-D convolution process in the form of 2-D matrix multiplication [52], [53], i.e.,

$$\mathbf{F} = \mathbf{A} \cdot \mathbf{I}, \quad (1)$$

where  $\mathbf{F} \in \mathbb{R}^{M \times B' \times H' \times W'}$  is the matrix form of  $\mathcal{F}$ ,  $\mathbf{A} \in \mathbb{R}^{M \times k^3 C}$  is the kernel matrix derived by flattening each of the 3-D kernels as a row vector and then vertically stacking them together (as illustrated in Fig. 1(a)), and  $\mathbf{I} \in \mathbb{R}^{k^3 C \times B' \times H' \times W'}$  denotes the matrix form of  $\mathcal{I}$  obtained by iteratively unrolling it along the spatial-spectral directions.

Considering that the rank of a 2-D matrix indicates the independence/freedom of its elements, we analyze the rank of the feature matrix  $\mathbf{F}$  to quantitatively measure its diversity. Specifically, based on the property of matrix multiplication, from Eq. (1), we have

$$\text{Rank}(\mathbf{F}) \leq \min\{\text{Rank}(\mathbf{A}), \text{Rank}(\mathbf{I})\}, \quad (2)$$

where  $\text{Rank}(\cdot)$  returns the rank of an input 2-D matrix. As the values of  $M$  and  $C$  are usually at the same level, we have  $M \ll k^3 C \ll B' \times H' \times W'$ , resulting in  $\text{Rank}(\mathbf{F}) \leq M$ . Therefore, relieving the upper bound of  $\text{Rank}(\mathbf{F})$ , which is fundamentally limited by that of  $\text{Rank}(\mathbf{A})$ , is the prerequisites to promote the learning of diverse and powerful features. To this end, we propose to raise the upper bound of  $\text{Rank}(\mathbf{A})$  by altering the network topology directly, i.e., structure-level feature diversity enhancement (Section

3.2). Besides, considering that a large proportion of kernel weights tend to converge to a marginal set of principal components during back-propagation [54], [55], [56], we further explicitly regularize the feature matrix  $\mathbf{F}$  to make it deviate from an approximately low-rank one, i.e., content-level feature diversity enhancement (Section 3.3).

#### 3.2 Structure-level Feature Diversity Enhancement

As shown in Fig. 1 (a), the convolutional kernels contained in a typical 3-D convolutional layer is flattened into a fat 2-D matrix  $\mathbf{A} \in \mathbb{R}^{M \times k^3 C}$ , the rank of which is upper bounded by  $M$ . Generally, we relieve such a limitation by permuting the elements of  $\mathbf{A}$  into a larger 2-D matrix with a higher rank upper bound, which can be further realized by a typical convolution manner. Note that as the three dimensions of HS images are equally essential [17], [57], we process the three dimensions indiscriminately to ensure that an identical convolution pattern could be finally applied to the three dimensions (i.e., the symmetry property).

Technically, we first construct a larger kernel matrix  $\mathbf{A}_a \in \mathbb{R}^{3LM \times k^3 C}$  by scaling up the number of channels by  $3L$  ( $L$  is a positive integer), i.e., each of the three dimensions is equipped with  $LM$  channels. Accordingly, we can rewrite the convolution process as

$$\mathbf{F}_a = \mathbf{A}_a \cdot \mathbf{I} \quad \text{with} \quad \mathbf{A}_a = [\mathbf{A}_a^1; \mathbf{A}_a^2; \mathbf{A}_a^3], \quad (3)$$

where  $\mathbf{F}_a \in \mathbb{R}^{3LM \times B' \times H' \times W'}$  denotes the resulting feature volume, and  $\{\mathbf{A}_a^i \in \mathbb{R}^{LM \times k^3 C}\}_{i=1}^3$  are the kernel matrices corresponding to the three dimensions of HS images. We expect that  $\mathbf{A}_a$  corresponds a typical convolution manner with the number of parameters not exceeding that of 3D convolution (i.e., the number of elements in  $\mathbf{A}$ ), which requires that  $\mathbf{A}_a$  has to be replenished with a certain number of zeros. Moreover, we obtain that the maximum number of parameters involved in each convolutional kernel is  $\frac{k^3 C}{3L}$ . Besides, we expect that resulting kernel matrix  $\mathbf{A}_a$  can be easily realized by commonly used convolution patterns. More specifically, we select the widely disseminated *regular* 1-D/2-D convolution as the desired alternatives. In the following we take the case that  $k = 3$  ( $k^3 = 27$  and  $\frac{k^3 C}{3L} = \frac{9C}{L}$ ) as an example for convenience. A larger convolutional kernel could be approximated by sequentially aggregating multiple layers with small kernels.

Based on the above conditions, when  $L = 1$ , we can deduce one feasible  $\mathbf{A}_a$  with the rank upper bound *minimally* raised to  $3M$ , as depicted in Fig. 1 (b), where the colored blocks indicate the distribution of network parameters. And such a kernel matrix can be realized by separately applying 2-D convolution of size  $3 \times 3$  along the three dimensions. When  $L = 3$ , as illustrated in Fig. 1 (c), we can construct a feasible  $\mathbf{A}_a$  with the rank upper bound *maximally* boosted to  $9M$ , which corresponds to the process of performing three 1-D convolution of size 3 in each of the three dimensions. For the above two feasible solutions, the number of kernel weights in  $\mathbf{A}_a$  is equal to that in  $\mathbf{A}$ . Alternatively, we can also construct feasible  $\mathbf{A}_a$  with a higher rank upper bound but fewer parameters to save computational costs. Specifically, as shown in Fig. 1 (d), when  $L = 1$  (resp.  $L = 2$ ), we can build  $\mathbf{A}_a$  with the rank upper bound equal to  $3M$  (resp.  $6M$ ), which can be achieved by separately

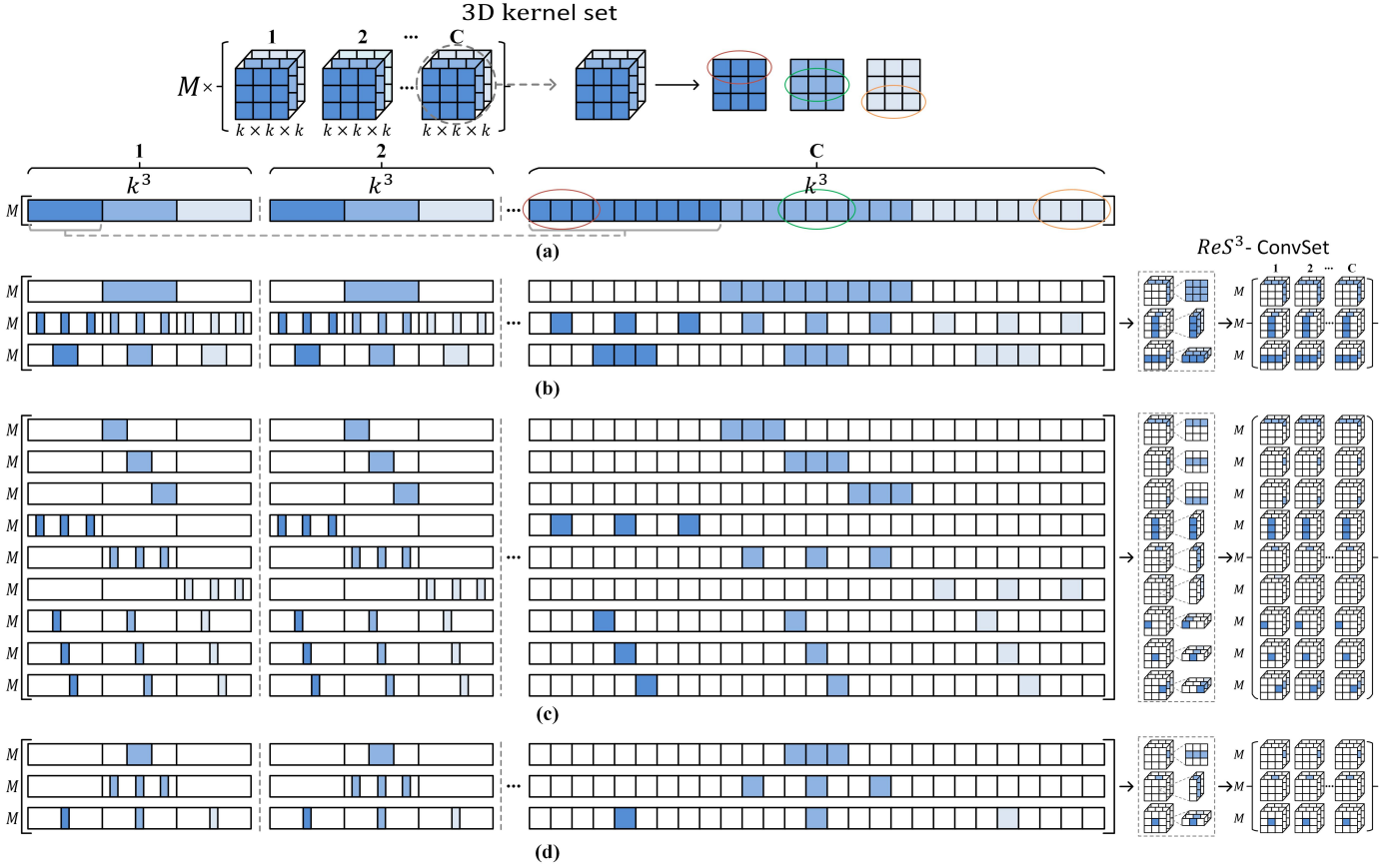


Fig. 1. Illustration of re-permuting the 3-D convolutional kernel set (a) into rank-enhanced spatial-spectral symmetrical patterns with different rank upper-bounds in (b), (c), and (d). Specifically, The colored cubes symbolize the kernel weights, whereas the blank ones represent replenished zeros. (a) the unrolled 3-D convolutional kernel matrix with the kernel size of 3. Meanwhile, (b), (c), and (d) represent to re-permute 3-D convolutional kernel matrix in our rank-enhanced spatial-spectral symmetrical manner with the kernel size of  $3 \times 3$ ,  $1 \times 3$ , and  $1 \times 3$ , of which the scaling factors are 3, 9, and 3, individually.

applying a single (resp. two) 1-D convolution of size 3 to each dimension.

Based on the above analyses, we can construct  $\mathbf{A}_a$ , whose rank upper bound varies from  $3M$  to  $9M$  without introducing extra parameters, thus potentially promoting the diversity of  $\mathbf{F}_a$ . Moreover, in light of the observation that the convolutional kernels for realizing  $\mathbf{A}_a$  with the rank upper bound equal to  $6M$  or  $9M$  share a similar pattern and receptive field to that for the case in Fig. 1 (d), they may only result in homogeneous feature content and a minor increase in feature diversity, which is also experimentally demonstrated, i.e., a larger rank upper bound than  $3M$  only brings marginal performance improvement (see Table 8). Thus, we finally adopt the permutation manner in Fig. 1 (d), i.e., separately performing 1-D convolution along the three dimensions, which can not only learn diverse spatial-spectral feature representations but also save network parameters.

### 3.3 Content-level Feature Diversity Enhancement

Despite that the upper-bound of  $\text{Rank}(\mathbf{F})$  has been raised via kernel matrix re-permutation, it is still theoretically potential that the diversity of the resulting features  $\mathbf{F}_a$  may not be fully enhanced. Specifically, previous studies [54], [55], [56] demonstrate that a large proportion of kernel weights tend to converge to a marginal set of principal components

during back-propagation. Thus, given a 2-D feature matrix with singular values of  $\{a_i\}_{i=1}^d$  that have been boosted to  $\{b_i\}_{i=1}^{nd}$ , the following case, i.e., a long-tail distribution of singular values, may exist:  $b_i \approx a_i$  ( $i \in [1, d]$ ), and  $a_i \gg b_j > 0$  ( $i \in [1, d], j \in [d+1, nd]$ ). The marginal magnitudes of the additional singular values  $\{b_j\}_{j=d+1}^{nd}$  are insufficient to bring remarkable merits, even though the re-permuted feature matrix has a much higher rank. In other words, the resulting  $\mathbf{F}_a$  may be approximately low-rank. In view of this issue, we further regularize the feature matrix  $\mathbf{F}_a$  directly to enhance its diversity by minimizing the following loss:

$$\mathcal{L}_p = -\|\text{SVD}(\mathbf{F}_a)\|_1, \quad (4)$$

where  $\text{SVD}(\cdot)$  returns a vector of singular values of an input 2-D matrix, and  $\|\cdot\|_1$  is the  $\ell_1$  norm.

Such a regularization term will narrow the gaps between large singular values and small ones to promote them to be uniformly distributed, which prevents  $\mathbf{F}_a$  from being an approximately low-rank matrix and likewise increases the freedom (or diversity) of its elements. Note that we only apply this regularization term at the last layer of the network before the final output to avoid introducing excessively high computational costs.



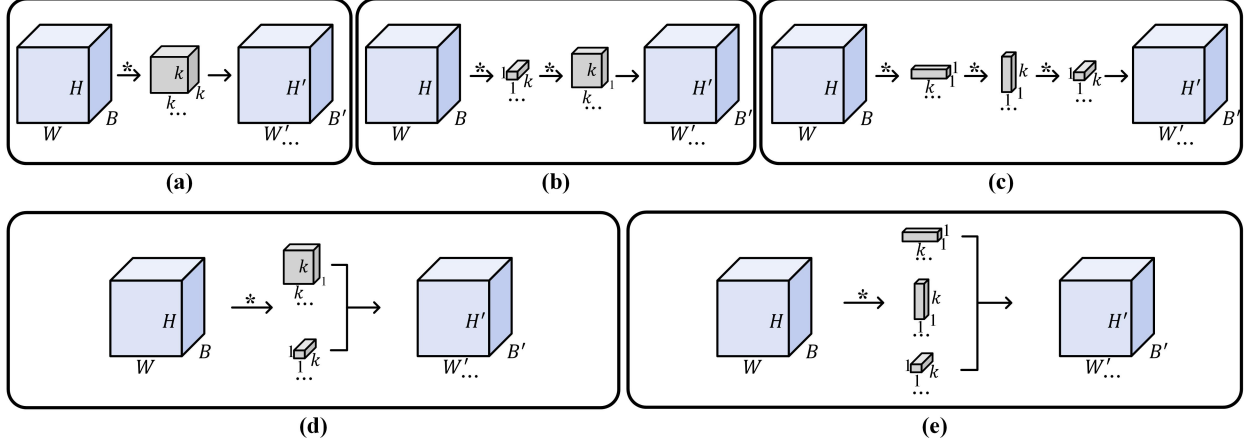


Fig. 2. Illustration of various feature extraction manners for HS images. (a) 3-D convolution, (b) Sequential 1-D and 2-D convolution, (c) Sequential 1-D convolution, (d) 1-D + 2-D convolution, and (e) Proposed ReS<sup>3</sup>-ConvSet.

### 3.4 More Analysis

We also analyze existing feature extraction methods for HS images by using our formulation to get a thorough understanding of them from the perspective of feature diversity, including “Sequential 1-D and 2-D convolution” in Fig. 2 (b), “Sequential 1-D convolution” in Fig. 2 (c), and “1-D + 2-D convolution” in Fig. 2 (d).

1) We can write the process of “Sequential 1-D and 2-D convolution” in the form of matrix multiplication:

$$\mathbf{F}_{s1d2d} = \mathbf{A}_{2d} \cdot \mathbf{I}_{1d}, \quad \mathbf{F}_{1d} = \mathbf{A}_{1d} \cdot \mathbf{I}, \quad (5)$$

where  $\mathbf{F}_{s1d2d} \in \mathbb{R}^{M \times B' H' W'}$  is the 2-D matrix form of the output feature maps;  $\mathbf{F}_{1d} \in \mathbb{R}^{M \times B' H' W'}$  denotes the matrix form of the intermediate feature maps by 1-D convolution;  $\mathbf{I}_{1d} \in \mathbb{R}^{k^3 M \times B' H' W'}$  symbolizes the local patches via sliding 2-D kernels over  $\mathbf{F}_{1d}$ ; and  $\mathbf{A}_{1d}$  and  $\mathbf{A}_{2d} \in \mathbb{R}^{M \times k^3 M}$  are the matrices of 1-D and 2-D kernels, respectively.

2) The convolution process of “Sequential 1-D convolution” can be phrased as

$$\mathbf{F}_{s1d} = \mathbf{A}_{1d3} \cdot \mathbf{I}_{1d2}, \quad \mathbf{F}_{1d2} = \mathbf{A}_{1d2} \cdot \mathbf{I}_{1d1}, \quad \mathbf{F}_{1d1} = \mathbf{A}_{1d1} \cdot \mathbf{I}, \quad (6)$$

Here,  $\mathbf{F}_{1d1}, \mathbf{F}_{1d2}, \mathbf{F}_{s1d} \in \mathbb{R}^{M \times B' H' W'}$  indicate the output feature maps of three sequentially aggregated convolutional layers,  $\mathbf{I}_{1d1}, \mathbf{I}_{1d2} \in \mathbb{R}^{k^3 M \times B' H' W'}$  represent local patch of corresponding feature maps in matrix forms,  $\mathbf{A}_{1d1}, \mathbf{A}_{1d2}, \mathbf{A}_{1d3} \in \mathbb{R}^{M \times k^3 M}$  are the matrices of corresponding 1-D kernels, respectively.

3) The convolution process of “1-D + 2-D convolution” can be written as

$$\mathbf{F}_{1d2d} = \mathbf{A}_{1d2d} \cdot \mathbf{I}, \quad \text{with } \mathbf{A}_{1d2d} = [\mathbf{A}_{2d}; \mathbf{A}_{1d}], \quad (7)$$

where  $\mathbf{F}_{1d2d} \in \mathbb{R}^{2M \times B' H' W'}$  encodes the output feature maps;  $\mathbf{A}_{1d2d} \in \mathbb{R}^{2M \times k^3 M}$  denotes the matrix of combined 1-D and 2-D kernels.

According to Eqs. (5), (6) and (7), we have  $\text{Rank}(\mathbf{F}_{s1d2d}) \leq M$ ,  $\text{Rank}(\mathbf{F}_{s1d}) \leq M$ , and  $\text{Rank}(\mathbf{F}_{1d2d}) \leq 2M$ . That is, these feature extraction manners expand the rank upper bound from  $M$  to  $2M$  at most, which is still limited. We refer the readers to Tables 9, 10, and 11 for the quantitative results of all the variants

illustrated in Fig. 2.

**Remarks.** For the feature extraction manner involving parallel branches, e.g., Figs. 2 (d) and (e), we utilize a  $1 \times 1 \times 1$  convolutional layer to compress the multiple output feature volumes before feeding it into the subsequent layer in order to avoid channel explosion. Thus, the feature volumes extracted by different convolution manners are finally with the equal size, i.e., the rank upper bounds of finally-output feature matrices are equal. However, our ReS<sup>3</sup>-ConvSet can boost the rank upper bound of feature matrix  $\mathbf{F}$  from  $M$  to  $3M$  during the feature extraction process, thus potentially promoting more diverse features. We refer the readers to Fig. 12 for the comparison of singular value distributions of the feature maps extracted by various convolution manners, where it can be clearly seen that the singular values of the feature matrix by our ReS<sup>3</sup>-ConvSet decrease more slowly than those of other schemes, indicating that our ReS<sup>3</sup>-ConvSet can balance the singular values to avoid only a few large ones dominating the feature space (i.e., the degree of freedom of entries of the feature matrix that is approximately low-rank is limited), thus promoting feature diversity.

## 4 APPLICATIONS

In this section, to demonstrate the advantages of the proposed ReS<sup>3</sup>-ConvSet and DA-Reg, we construct three learning-based methods for HS image denoising, spatial super-resolution, and classification. Note that we mainly incorporate ReS<sup>3</sup>-ConvSet into existing frameworks to directly demonstrate their advantages.

### 4.1 HS Image Denoising

Let  $\mathcal{X}_n \in \mathbb{R}^{B \times H \times W}$  be a noisy HS image, and  $\mathcal{Y} \in \mathbb{R}^{B \times H \times W}$  the corresponding noise-free one, where  $H$  and  $W$  are the spatial dimensions, and  $B$  is the number of spectral bands. The degradation process of  $\mathcal{Y}$  to  $\mathcal{X}_n$  could be generally formulated as

$$\mathcal{X}_n = \mathcal{Y} + \mathcal{N}_z, \quad (8)$$

where  $\mathcal{N}_z \in \mathbb{R}^{B \times H \times W}$  denotes the additive noise.

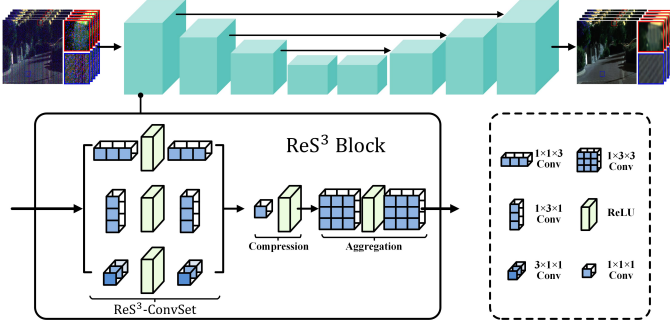


Fig. 3. Illustration of our HS image denoising framework, which is constructed by incorporating the proposed  $\text{ReS}^3\text{-ConvSet}$  into a residual U-Net architecture.

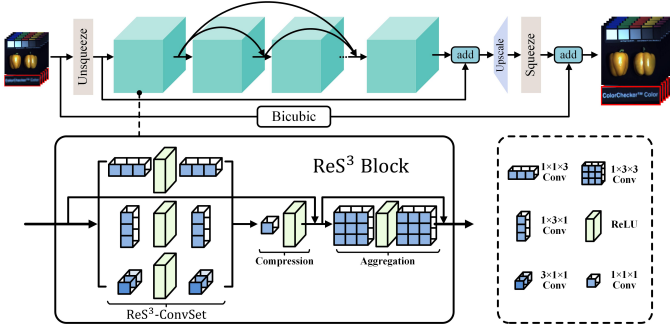


Fig. 4. Illustration of our HS image super-resolution framework, which is constructed by incorporating the proposed  $\text{ReS}^3\text{-ConvSet}$  into a residual-dense architecture.

We incorporate the proposed  $\text{ReS}^3\text{-ConvSet}$  into the widely-used U-Net [58] architecture for constructing an efficient and compact HS image denoising method. As illustrated in Fig. 3, the denoising framework is composed of multiple  $\text{ReS}^3$  blocks. In each block,  $\text{ReS}^3\text{-ConvSet}$  separately performs 1-D convolution along the three dimensions of an HS image, and a compression layer and an aggregation layer are adopted to aggregate the resulting spatial-spectral embeddings.

We train the denoising network by jointly minimizing the  $\ell_1$  distance between the recovered HS image  $\hat{\mathcal{Y}}_d$  and  $\mathcal{Y}$  and the proposed DA-Reg:

$$\mathcal{L}_d = \mathcal{L}_1(\hat{\mathcal{Y}}_d, \mathcal{Y}) + \lambda \mathcal{L}_p, \quad (9)$$

where the hyper-parameter  $\lambda$  is empirically set to  $1 \times 10^{-4}$ .

## 4.2 HS Image Spatial Super-resolution

Given a low-spatial-resolution HS image denoted as  $\mathcal{X}_{lr} \in \mathbb{R}^{B \times h \times w}$  with  $h \times w$  being the spatial dimensions, we aim to recover a high-spatial-resolution HS image denoted as  $\mathcal{Y} \in \mathbb{R}^{B \times H \times W}$ , in which  $H = \alpha h$  and  $W = \alpha w$  ( $\alpha > 1$  is the scale factor). The degradation process of  $\mathcal{X}_{lr}$  from  $\mathcal{Y}$  can be generally formulated as

$$\mathcal{X}_{lr} = \mathcal{D}(\mathcal{Y}) + \mathcal{N}_z, \quad (10)$$

where  $\mathcal{D}(\cdot)$  is the degeneration operator, consisting of the down-sampling and blurring operations.

For HS image spatial super-resolution, as shown in Fig. 4, we embed the proposed method into the popular residual dense architecture [59] to construct an HS image super-resolution framework that includes several  $\text{ReS}^3$

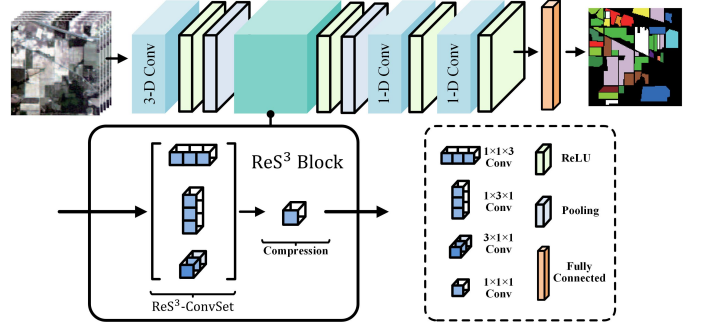


Fig. 5. Illustration of our HS image classification framework, which is constructed by incorporating the proposed  $\text{ReS}^3\text{-ConvSet}$  into the existing method [9].

blocks. Each block is devised utilizing residual learning, containing a  $\text{ReS}^3\text{-ConvSet}$ , a compression layer, and an aggregation layer. We train the super-resolution framework by simultaneously minimizing the  $\ell_1$  distance between the super-resolved HS image  $\hat{\mathcal{Y}}_{sr}$  and  $\mathcal{Y}$ , and the proposed DA-Reg. The overall loss function is written as

$$\mathcal{L}_{sr} = \mathcal{L}_1(\hat{\mathcal{Y}}_{sr}, \mathcal{Y}) + \lambda \mathcal{L}_p, \quad (11)$$

where the value of  $\lambda$  is empirically set to  $1 \times 10^{-7}$ .

## 4.3 HS Image Classification

For HS image classification, we incorporate the proposed method into the existing method [9] to construct the classification framework, as shown in Fig. 5, it consists of one  $\text{ReS}^3$  block and three conventional filters, i.e., a 3-D convolution for obtaining the basic HS features, and two 1-D convolutions for pooling in the spectral domain. We train the classification network by simultaneously optimizing the cross entropy loss between predicted labels and ground-truth ones and our DA-Reg, i.e.,

$$\mathcal{L}_c = \mathcal{L}_{ce} + \lambda \mathcal{L}_p, \quad (12)$$

where the value of  $\lambda$  is empirically set to  $1 \times 10^{-4}$ .

## 5 EXPERIMENTS

### 5.1 Evaluation on HS Image Denoising

#### 5.1.1 Experiment settings

**Datasets.** We employed two commonly-used HS image benchmark datasets for evaluation, including one natural HS image dataset, i.e., ICVL<sup>1</sup> [65], and one remote sensing HS image, i.e., Urban<sup>2</sup>. Specifically, ICVL consists of 201 HS images of spatial dimensions  $1392 \times 1300$  and spectral dimension 31 covering the wavelength in the range of 400 to 700 nm, acquired by a Specim PS Kappa DX4 HS camera. We utilized 100 HS images as the training set, and the rest as the testing set. Urban contains  $307 \times 307$  pixels and 210 spectral bands collected by the HYDICE hyperspectral system. This image is corrupted by *real unknown noise* and widely used for real HS image denoising testing.

Following previous works [6], [25], we considered two types of noise settings, i.e., the Gaussian noise and the

1. <http://icvl.cs.bgu.ac.il/hyperspectral/>  
2. <https://rslab.ut.ac.ir/data>

TABLE 1

Quantitative comparisons of different methods under several noise levels over the ICVL dataset. The best and second best results are highlighted in bold and underline, respectively. “ $\uparrow$ ” (resp. “ $\downarrow$ ”) means the larger (resp. smaller), the better.

$\sigma$	Metrics	Methods									
		Noisy	LRRM [60]	NMoG [61]	LRTDTV [62]	ITSReg [63]	GRN [6]	QRNN3D [25]	NG-Meet [64]	T3SC [28]	ReS <sup>3</sup> Net
30	MPSNR $\uparrow$	18.59	32.96	33.24	38.43	41.53	41.83	42.28	43.09	<u>43.19</u>	<b>43.76</b>
	MSSIM $\uparrow$	0.1034	0.7247	0.7464	0.9365	0.9571	0.9653	0.9701	0.9709	<u>0.9718</u>	<b>0.9750</b>
	SAM $\downarrow$	0.7269	0.2298	0.1537	0.0835	0.0929	0.0541	0.0617	<u>0.0491</u>	0.0616	<b>0.0449</b>
50	MPSNR $\uparrow$	14.15	28.98	29.98	36.47	39.19	38.84	40.22	40.35	<u>40.81</u>	<b>41.48</b>
	MSSIM $\uparrow$	0.0429	0.5400	0.5900	0.9159	0.9350	0.9422	0.9544	0.9541	<u>0.9567</u>	<b>0.9611</b>
	SAM $\downarrow$	0.9096	0.3223	0.1895	0.1043	0.0841	0.1010	0.0733	<u>0.0582</u>	0.0720	<b>0.0538</b>
70	MPSNR $\uparrow$	11.23	26.38	27.80	34.97	37.48	37.22	38.29	38.71	<u>39.27</u>	<b>39.93</b>
	MSSIM $\uparrow$	0.0228	0.4160	0.4836	0.8971	0.9192	0.9264	0.9326	0.9414	<u>0.9431</u>	<b>0.9484</b>
	SAM $\downarrow$	1.0273	0.3955	0.2200	0.1201	0.1144	0.0853	0.0943	<u>0.0639</u>	0.0810	<b>0.0611</b>
Blind	MPSNR $\uparrow$	14.83	29.57	30.48	36.76	39.52	39.21	40.48	40.89	<u>40.98</u>	<b>41.81</b>
	MSSIM $\uparrow$	0.0534	0.5674	0.6146	0.9190	0.9389	0.9452	0.9559	<u>0.9579</u>	<u>0.9579</u>	<b>0.9630</b>
	SAM $\downarrow$	0.8800	0.3060	0.1823	0.1012	0.1037	0.0717	0.0737	<u>0.0568</u>	0.0723	<b>0.0531</b>

TABLE 2

Quantitative comparisons of different methods under five complex noise cases over the ICVL dataset. The best and second best results are highlighted in bold and underline, respectively. “ $\uparrow$ ” (resp. “ $\downarrow$ ”) means the larger (resp. smaller), the better.

Case	Metrics	Methods									
		Noisy	NG-Meet [64]	LRRM [60]	NMoG [61]	ITSReg [63]	LRTDTV [62]	GRN [6]	QRNN3D [25]	T3SC [28]	ReS <sup>3</sup> Net
1	MPSNR $\uparrow$	17.80	28.62	28.64	34.96	36.02	37.95	39.97	42.79	<u>43.51</u>	<b>44.33</b>
	MSSIM $\uparrow$	0.1516	0.5764	0.5153	0.8279	0.8451	0.9377	0.9587	0.9752	<u>0.9776</u>	<b>0.9800</b>
	SAM $\downarrow$	0.7911	0.4301	0.3235	0.1260	0.1408	0.0671	0.0685	<u>0.0430</u>	0.0441	<b>0.0327</b>
2	MPSNR $\uparrow$	17.77	28.15	28.52	34.60	35.35	37.65	39.90	42.64	<u>43.20</u>	<b>44.35</b>
	MSSIM $\uparrow$	0.1545	0.5576	0.5155	0.8184	0.8210	0.9348	0.9598	0.9750	<u>0.9770</u>	<b>0.9805</b>
	SAM $\downarrow$	0.7895	0.4401	0.3250	0.1793	0.1525	0.0731	0.0672	<u>0.0437</u>	0.0488	<b>0.0331</b>
3	MPSNR $\uparrow$	17.36	27.69	27.78	33.60	32.68	35.67	38.74	<u>42.31</u>	41.42	<b>44.33</b>
	MSSIM $\uparrow$	0.1473	0.5703	0.5075	0.8212	0.7879	0.9181	0.9548	<u>0.9735</u>	0.9724	<b>0.9802</b>
	SAM $\downarrow$	0.8109	0.4443	0.3398	0.1885	0.1812	0.0937	0.0702	<u>0.0455</u>	0.0639	<b>0.0330</b>
4	MPSNR $\uparrow$	14.86	25.32	24.19	29.09	26.47	36.60	37.63	<u>40.49</u>	37.93	<b>42.59</b>
	MSSIM $\uparrow$	0.1118	0.5211	0.3805	0.6751	0.5019	0.9265	0.9410	<u>0.9533</u>	0.9353	<b>0.9668</b>
	SAM $\downarrow$	0.8480	0.5814	0.4681	0.4510	0.4818	0.0874	0.0952	<u>0.0762</u>	0.1669	<b>0.0595</b>
5	MPSNR $\uparrow$	14.07	24.33	23.79	28.45	25.02	34.51	38.01	<u>39.42</u>	35.84	<b>41.94</b>
	MSSIM $\uparrow$	0.0936	0.4964	0.3817	0.6746	0.4871	0.9076	<u>0.9473</u>	0.9448	0.9248	<b>0.9644</b>
	SAM $\downarrow$	0.8587	0.5874	0.4668	0.4568	0.4830	0.1063	0.0904	<u>0.0809</u>	0.1804	<b>0.0622</b>

complex noise, which were applied to ICVL dataset to simulate noisy HS images. Specifically, for the Gaussian noise, we set various noise levels, i.e.,  $\sigma = 30, 50, 70$ , and “Blind (the value of  $\sigma$  is in the range of 30 to 70 but unknown)”. We generated five types of complex noises to imitate the real-world noise cases, including Non-i.i.d. Gaussian Noise, Gaussian and Stripe Noise, Gaussian and Deadline Noise, Gaussian and Impulse Noise, and Mixture Noise, referred as “Case 1” to “Case 5”. We refer the readers to [6], [25] for more details about the noise settings.

**Implementation details.** We implemented all the experiments with PyTorch on a PC with NVIDIA GeForce RTX 3080 GPU, Intel(R) Core(TM) i7-10700 CPU of 2.90GHz and 64-GB RAM. We employed the ADAM optimizer [66] with the exponential decay rates  $\beta_1 = 0.9$  and  $\beta_2 = 0.999$ . The total training process was 25 epochs for both two kinds of noise experiments. We initialized the learning rate as  $5 \times 10^{-4}$ , which was halved every 5 epochs. We set the batch size to 4 in all experiments.

TABLE 3

Comparisons of #Param, #FLOPs, and inference time of deep learning-based HS image denoising methods on the ICVL dataset. Since T3SC [28] was built based on sparse coding and deep learning, we could not calculate the #FLOPs like other pure deep learning-based methods.

Methods	GRN	QRNN3D	T3SC	ReS <sup>3</sup> Net
#Param (M)	1.07	0.86	0.83	0.66
#FLOPs (T)	0.22	1.26	-	0.95
Inference time (s)	0.23	0.52	1.93	0.77

### 5.1.2 Comparison with state-of-the-art methods

We compared the proposed denoising method with three state-of-the-art deep learning-based methods, i.e., QRNN3D [25], GRN [6], and T3SC [28], and five representative non-learning-based methods, including LRRM [60], ITSReg [63], NMoG [61], LRTDTV [62], NG-Meet [64]. Note that for QRNN3D [25], GRN [6], and our method, only a single network was trained for each noise setting, i.e., a single network for handling noisy HS images with different Gaussian noise levels (or complex noises); while for T3SC



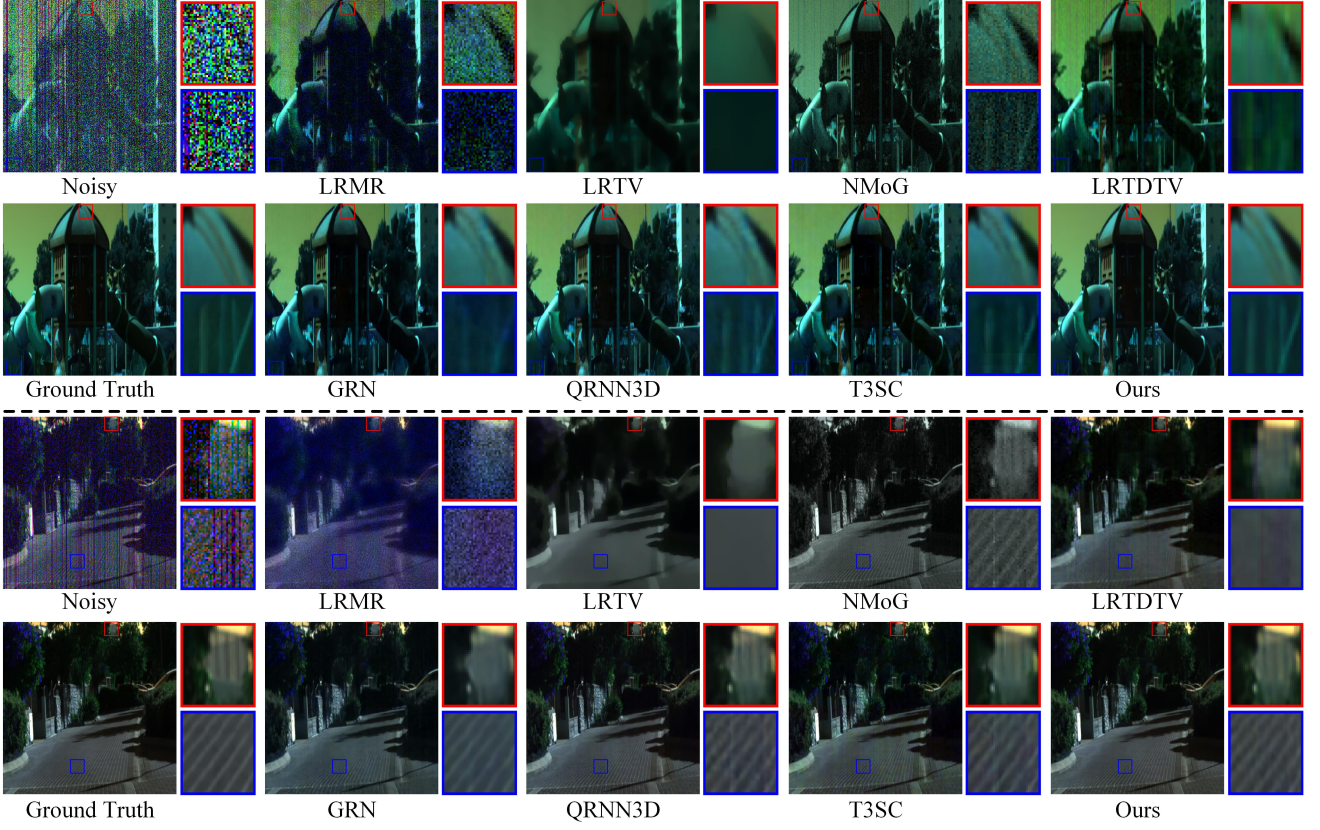


Fig. 6. Visual comparison of different methods on *ICVL* with Gaussian and deadline, and mixture noise, from top to bottom. Here, we selected the 5<sup>th</sup>, 16<sup>th</sup>, and 30<sup>th</sup>, and 10<sup>th</sup>, 17<sup>th</sup>, and 30<sup>th</sup>) bands to form a pseudo RGB image to enable the visualization under Gaussian and deadline noise (resp. mixture noise).

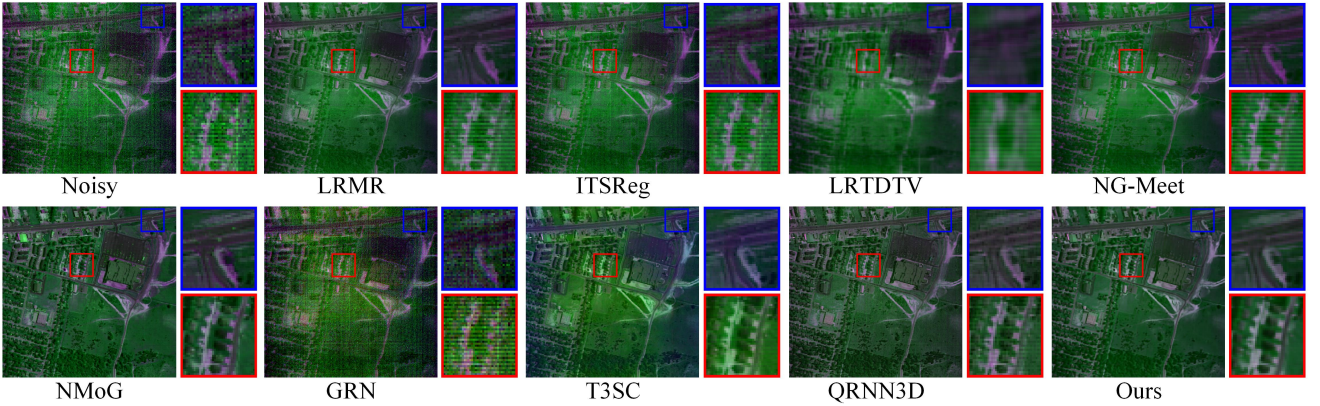


Fig. 7. Visual comparison of different methods on *Urban* with real unknown noise. Here we selected the 38<sup>th</sup>, 112<sup>nd</sup>, and 128<sup>th</sup> bands to form a pseudo RGB image to enable the visualization.

[28], a network was trained for each case of the two types of noise settings, i.e., nine networks for the four Gaussian noises and five complex noises. In other words, the comparison setting is more favorable for T3SC.

**Quantitative comparison.** We adopted three commonly used quantitative metrics to evaluate the quality of the denoised HS images, i.e., Mean Peak Signal-to-Noise Ratio (MPSNR), Mean Structural Similarity Index (MSSIM) [68], and Spectral Angle Mapper (SAM) [69]. Tables 1 and 2 show the quantitative results of different methods, where it can be observed that our method consistently achieves the best performance in terms of all the three metrics under all noise

scenarios. Particularly, our method improves the MPSNR of the second best methods by 0.57 dB, 0.67 dB, 0.66 dB, and 0.83 dB under four Gaussian noise levels, and 0.82 dB, 1.15 dB, 2.02 dB, 2.10 dB, and 2.52 dB under five types of complex noises, respectively. Besides, the impressive performance of our method under both the blind Gaussian noise and all the complex noise scenarios demonstrates that it has better resilience on severely corrupted HS images; and

**Visual comparison.** Fig. 6 shows the visual comparisons of denoising results by different methods on *ICVL*, where we can observe that the denoised images by our method is cleaner and retain the original high-frequency details better. In addition, Fig. 7 provides the visual comparisons



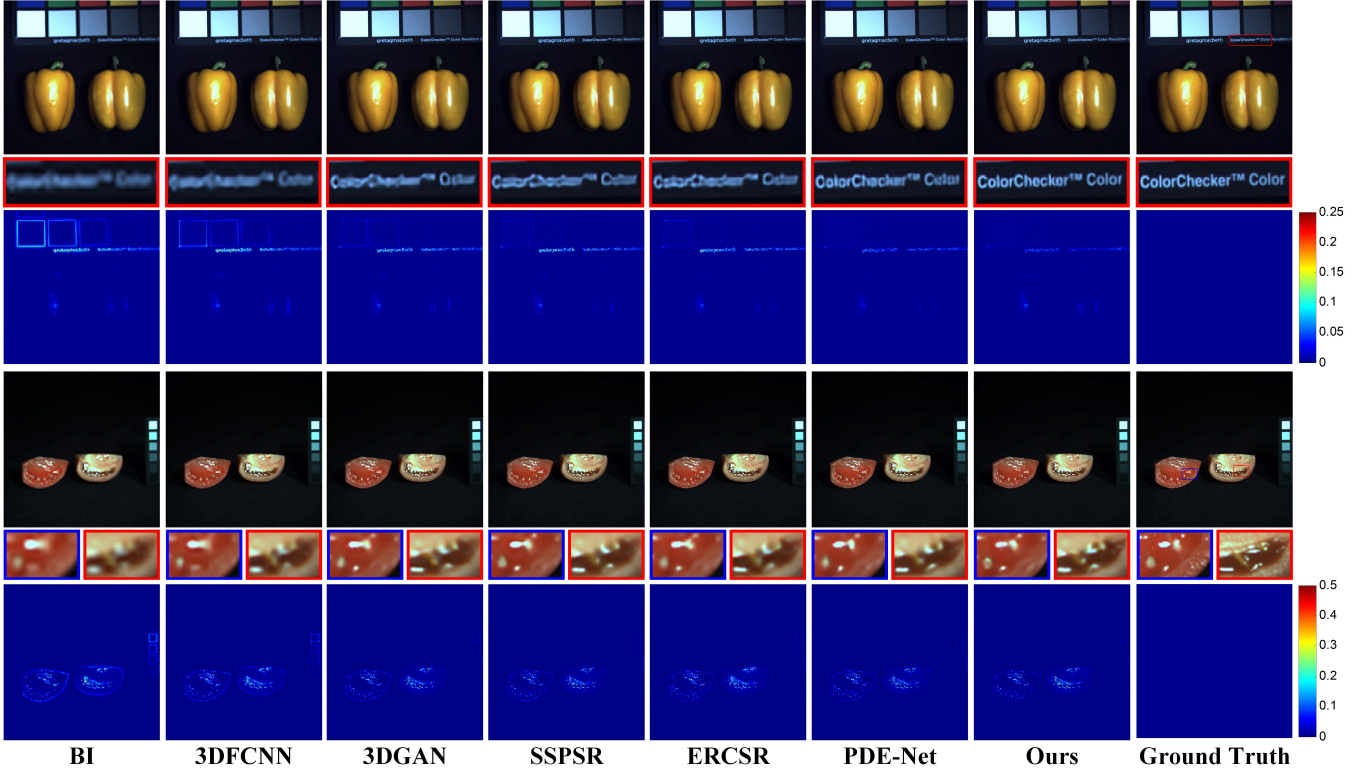


Fig. 8. Visual comparisons of different methods with  $\alpha = 4$  over CAVE dataset. For ease of comparison, we visualized the reconstructed HS images in the form of RGB images, which were generated via employing the commonly-used spectral response function of Nikon-D700 [67].

of denoised HS images by different methods on Urban, a real-world noisy HS image, where we can see that most of the compared methods fail to remove the unknown noise completely. By contrast, our method successfully tackles this unknown noise and produces a clearer and visually pleasing image.

**Computational efficiency.** We compared the number of network parameters (#Param), floating point of operations (#FLOPs), and inference time of deep learning-based methods in Table 3, where it can be observed that our method consumes fewer network parameters and has comparable #FLOPs, and inference time, compared with state-of-the-art methods, demonstrating that the excellent performance of our method does not come at the cost of a larger capacity and higher computational complexity but is credited to the proposed ReS<sup>3</sup>-ConvSet and DA-Reg.

## 5.2 Evaluation on HS Image Spatial SR

### 5.2.1 Experiment settings

**Datasets.** We employed the commonly-used HS image benchmark dataset for evaluation, i.e., CAVE<sup>3</sup> [70], which contains 32 HS images of spatial dimensions  $512 \times 512$  and spectral dimension 31 covering the wavelength in the range of 400 to 700 nm, collected by a generalized assorted pixel camera. We randomly selected 20 HS images for training, and the remaining 12 HS images for testing.

**Implementation details.** We employed the ADAM optimizer [66] with the exponential decay rates  $\beta_1 = 0.9$  and

TABLE 4

Quantitative comparisons of different methods over the CAVE dataset. The best and second best results are highlighted in bold and underline, respectively. “↑” (resp. “↓”) means the larger (resp. smaller), the better.

Methods	Scale	#Params	MPSNR↑	MSSIM↑	SAM↓
BI	4	-	36.533	0.9479	4.230
3DFCNN [7]	4	0.04M	38.061	0.9565	3.912
3DGAN [30]	4	0.59M	39.947	0.9645	3.702
SSPSR [5]	4	26.08M	40.104	0.9645	3.623
ERCSR [32]	4	1.59M	40.701	0.9662	3.491
PDE-Net [35]	4	2.30M	41.236	<b>0.9672</b>	<u>3.455</u>
Ours	4	2.11M	<b>41.443</b>	<b>0.9672</b>	<b>3.412</b>
BI	8	-	32.283	0.8993	5.412
3DFCNN [7]	8	0.04M	33.194	0.9131	5.019
3DGAN [30]	8	0.66M	34.930	0.9293	4.888
SSPSR [5]	8	28.44M	34.992	0.9273	4.680
ERCSR [32]	8	2.38M	35.519	0.9338	4.498
PDE-Net [35]	8	2.33M	<u>36.021</u>	<u>0.9363</u>	<u>4.312</u>
Ours	8	2.31M	<b>36.257</b>	<b>0.9377</b>	<b>4.242</b>

$\beta_2 = 0.999$ . We initialized the learning rate as  $5 \times 10^{-4}$ , which was halved every 25 epochs. We set the batch size to 4. The total training process contained 50 warm-ups and 50 training epochs. During the warm-up phase, we trained our model by only minimizing the  $\ell_1$  loss, i.e.,  $\lambda = 0$ .

### 5.2.2 Comparison with state-of-the-art methods

We compared our HS image spatial super-resolution method with six state-of-the-art deep learning-based methods, i.e., 3DFCNN [7], 3DGAN [30], SSPSR [5], ERCSR [32], and PDE-Net [35]. We also provided the results of bi-cubic interpolation (BI) as a baseline.

3. <http://www.cs.columbia.edu/CAVE/databases/>

TABLE 5

Comparisons of the computational efficiency of different HS spatial SR methods on the CAVE dataset.

Methods	Scale	Inference time	#FLOPs	Scale	Inference time	#FLOPs
3DFCNN [7]	4	0.088s	0.321T	8	0.080s	0.321T
3DGAN [30]	4	0.369s	1.300T	8	0.332s	1.233T
SSPSR [5]	4	0.429s	3.029T	8	0.302s	1.818T
ERCSR [32]	4	0.380s	4.463T	8	0.283s	10.429T
PDE-Net [35]	4	0.526s	6.375T	8	0.207s	3.020T
Ours	4	0.463s	1.917T	8	0.195s	2.752T

TABLE 6

Quantitative performance of different classification methods in terms of OA, AA, and Kappa, as well as the accuracies for each class on the Indian Pines dataset. The best results are highlighted in bold.

Class No.	3-D CNN [9]	FuNet-C [47]	SpectralFormer [49]	Ours
1	<b>89.67</b>	67.19	68.64	86.92
2	82.02	78.70	<b>87.50</b>	85.20
3	86.96	<b>99.46</b>	85.33	92.39
4	<b>96.64</b>	95.75	95.75	95.75
5	91.82	93.69	85.80	<b>98.28</b>
6	98.17	<b>99.32</b>	97.49	<b>99.32</b>
7	80.39	79.19	<b>85.29</b>	63.51
8	61.49	69.77	76.92	<b>84.86</b>
9	80.85	70.57	78.90	<b>82.09</b>
10	<b>100.00</b>	99.38	99.38	<b>100.00</b>
11	93.41	89.79	93.25	<b>93.41</b>
12	96.96	94.24	81.82	<b>97.27</b>
13	97.78	<b>100.00</b>	<b>100.00</b>	97.78
14	89.74	87.18	71.79	<b>94.87</b>
15	<b>100.00</b>	<b>100.00</b>	<b>100.00</b>	<b>100.00</b>
16	<b>100.00</b>	<b>100.00</b>	<b>100.00</b>	<b>100.00</b>
OA	82.38	80.06	82.88	<b>87.17</b>
AA	90.37	89.01	87.99	<b>91.98</b>
Kappa	0.8004	0.7736	0.8047	<b>0.8524</b>

**Quantitative comparison.** Table 4 shows the quantitative results of different methods, where it can be observed that our method consistently achieves the best values in terms of all the three metrics under  $4\times$  and  $8\times$  spatial super-resolution tasks, validating the superiority of our proposed method. Besides, the network size of our method, validating that the satisfactory performance of our method is not achieved by piling up larger capacity but credited to elegant feature extraction technique.

**Visual comparison.** Fig. 8 visually compares the results of different methods, where it can be observed that the super-resolved images by our method present sharper and clearer textures and are closer to the ground truth ones, which further demonstrates its advantage.

**Computational efficiency.** Table 5 compares the computational efficiency of different approaches measured with the #FLOPs and inference time, where it can be observed that the proposed method consumes much fewer #FLOPs and less inference times than most compared methods.

### 5.3 Evaluation on HS Image Classification

#### 5.3.1 Experiment settings

**Datasets.** We employed the two commonly-used HS image classification benchmarks for evaluation, i.e., Indian Pines<sup>4</sup>, and Pavia University<sup>5</sup>. Specifically, Indian Pines is of spatial

4. <https://rslab.ut.ac.ir/data>

5. [http://www.ehu.es/ccwintco/index.php/Hyperspectral\\_Remote\\_Sensing\\_Scenes/](http://www.ehu.es/ccwintco/index.php/Hyperspectral_Remote_Sensing_Scenes/)

TABLE 7

Quantitative performance of different classification methods in terms of OA, AA, and Kappa, as well as the accuracies for each class on the Pavia University dataset. The best results are highlighted in bold.

Class No.	3-D CNN [9]	FuNet-C [47]	SpectralFormer [49]	Ours
1	79.71	80.08	<b>82.73</b>	82.09
2	95.69	94.28	94.03	<b>98.15</b>
3	<b>80.39</b>	67.66	73.66	77.74
4	<b>98.52</b>	97.80	93.75	96.35
5	99.82	99.19	99.28	<b>100.0</b>
6	85.89	91.49	<b>90.75</b>	82.17
7	84.91	85.93	87.56	<b>93.78</b>
8	97.24	96.64	95.81	<b>97.68</b>
9	94.88	<b>95.22</b>	94.21	94.09
OA	91.51	90.92	91.07	<b>92.56</b>
AA	90.70	89.81	90.20	<b>91.34</b>
Kappa	0.8858	0.8787	0.8805	<b>0.8994</b>

TABLE 8

Results of the ablation study towards different rank upper bounds of our ReS<sup>3</sup>-ConvSet over HS image super-resolution with  $\alpha = 4$  over CAVE dataset.

Methods	Rank upper bound	Kernel	# Params	MPSNR $\uparrow$	MSSIM $\uparrow$	SAM $\downarrow$
3-D	1M	3-D	3.59 M	40.98	0.9664	3.452
ReS <sup>3</sup> -ConvSet	3M	2-D	3.73 M	41.28	0.9669	3.423
ReS <sup>3</sup> -ConvSet	3M	1-D	2.11 M	41.35	0.9671	3.418
ReS <sup>3</sup> -ConvSet	6M	1-D	3.06 M	41.29	0.9671	3.415
ReS <sup>3</sup> -ConvSet	9M	1-D	4.00 M	41.32	0.9672	3.394

dimensions  $145 \times 145$  and spectral dimension 220 covering the wavelength in the range of 400 to 2500 nm, collected by the Airborne Visible/Infrared Imaging Spectrometer (AVIRIS) sensor. There are 16 mainly investigated categories in this studied scene. Following [47], [49], we employed 695 samples for training and 9671 samples for testing. Pavia University was gathered by the ROSIS sensor, consisting of  $610 \times 340$  pixels and 103 spectral bands from the range of 430 to 860 nm. There are 9 land cover categories. The number of samples utilized for training and testing is 3921 and 40002, respectively.

**Implementation details.** We employed the ADAM optimizer [66] with the exponential decay rates  $\beta_1 = 0.9$  and  $\beta_2 = 0.999$ . The total training process contained 1000 epochs for Indian Pines, and 150 epochs for Pavia University. We set the batch size to 64 and initialized the learning rate as  $1 \times 10^{-3}$ . We set the patch size as  $7 \times 7$  during training.

#### 5.3.2 Comparison with state-of-the-art methods

We compared our method with three state-of-the-art deep learning-based HS image classification methods named 3-D CNN [9], FuNet-C [47], and SpectralFormer [49]. Following existing methods, we adopted three widely-used metrics, i.e., Overall Accuracy (OA), Average Accuracy (AA), and Kappa Coefficient, to evaluate the HS image classification performance.

As listed in Tables 6 and 7, it can be seen that our method consistently achieves the highest accuracy in terms of OA, AA, and Kappa metrics on both Indian Pines and Pavia University, although some of the compared methods adopt more advanced deep learning strategies, such as, the fusion of CNN and GCN, and Transformer [71]. Besides, from Figs. 9 and 10, it can be seen that our method produces more accurate classification maps, again demonstrating its advantage.

TABLE 9

Results of the ablation study towards different convolution manners used for HS image denoising on the ICVL dataset with the Gaussian noise ( $\sigma = 70$ ).

Methods	#Params (M)	#FLOPs (T)	Rank upper bound	MPSNR $\uparrow$	MSSIM $\uparrow$	SAM $\downarrow$
3-D conv. (Fig. 2 (a))	1.201	1.562	$M$	39.34	0.9430	0.0693
Seq. 1-D conv. (Fig. 2 (c))	0.614	0.765	$M$	39.42	0.9430	0.0658
Seq. 1-D and 2-D conv. (Fig. 2 (b))	0.717	0.889	$M$	39.58	0.9445	0.0652
1-D + 2-D conv. (Fig. 2 (d))	0.740	1.082	$2M$	39.71	0.9459	0.0610
ReS <sup>3</sup> -ConvSet	0.658	0.953	$3M$	39.85	0.9478	0.0606

TABLE 10

Results of the ablation study towards different convolution manners used for  $4\times$  HS image spatial super-resolution on the CAVE dataset.

Methods	#Params (M)	#FLOPs (T)	Rank upper bound	MPSNR $\uparrow$	MSSIM $\uparrow$	SAM $\downarrow$
3-D conv. (Fig. 2 (a))	3.586	2.668	$M$	40.98	0.9664	3.452
Seq. 1-D conv. (Fig. 2 (c))	1.987	1.853	$M$	41.00	0.9668	3.430
Seq. 1-D and 2-D conv. (Fig. 2 (b))	2.269	1.997	$M$	41.10	0.9666	3.426
1-D + 2-D conv. (Fig. 2 (d))	2.332	2.029	$2M$	41.17	0.9667	3.418
ReS <sup>3</sup> -ConvSet	2.110	1.917	$3M$	41.35	0.9671	3.418

TABLE 11

Results of the ablation study towards different convolution manners used for HS image classification on *Indian Pines*.

Methods	#Params (M)	#FLOPs (G)	Rank upper bound	OA	AA	Kappa
3-D conv. (Fig. 2 (a))	0.395	0.0639	$M$	82.38	90.37	0.8004
Seq. 1-D conv. (Fig. 2 (c))	0.385	0.0406	$M$	82.61	90.09	0.8023
Seq. 1-D and 2-D conv. (Fig. 2 (b))	0.386	0.0419	$M$	82.94	89.51	0.8056
1-D + 2-D conv. (Fig. 2 (d))	0.387	0.0442	$2M$	83.83	90.97	0.8152
ReS <sup>3</sup> -ConvSet	0.386	0.0421	$3M$	85.32	91.86	0.8324

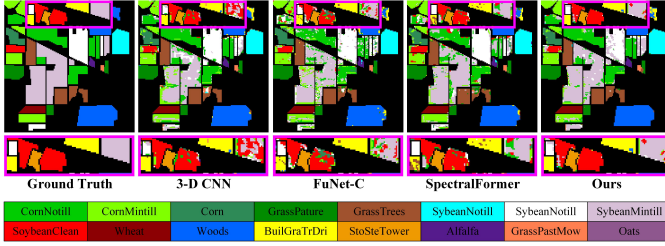


Fig. 9. Visual comparisons of the classification maps obtained by different methods on the Indian Pines dataset. Selected regions have been zoomed in for better comparison.

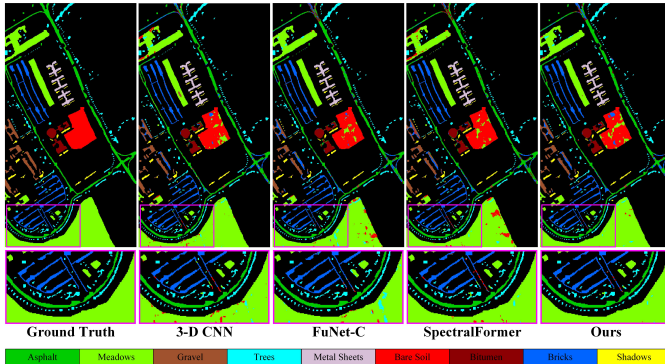


Fig. 10. Visual comparisons of the classification maps obtained by different methods on the Pavia University dataset. Selected regions have been zoomed in for better comparison.

## 5.4 Ablation Study

### 5.4.1 ReS<sup>3</sup>-ConvSet with different rank upper bounds

We compared our ReS<sup>3</sup>-ConvSet with different rank upper bounds in Table 8, where it can be observed that all cases

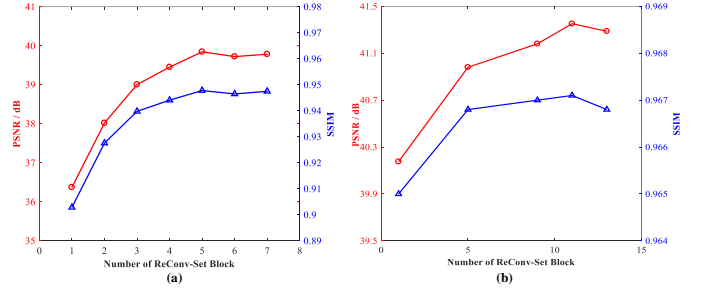


Fig. 11. Illustration of the effect of the number of ReS<sup>3</sup> block on the quantitative performance of (a) our HS image denoising method on the ICVL dataset with the Gaussian noise ( $\sigma = 70$ ), and (b) our  $4\times$  spatial SR method on the CAVE dataset.

TABLE 12

Results of the ablation study towards our ReS<sup>3</sup>-ConvSet and DA-Reg over HS image denoising on the ICVL dataset with the Gaussian noise ( $\sigma = 70$ ). For the first two settings, we replaced ReS<sup>3</sup>-ConvSet with 3-D convolution with an identical number of layers.

ReS <sup>3</sup> -ConvSet	DA-Reg	MPSNR $\uparrow$	MSSIM $\uparrow$	SAM $\downarrow$
$\times$	$\times$	39.34	0.9430	0.0693
$\times$	$\checkmark$	39.44	0.9435	0.0684
$\checkmark$	$\times$	39.85	0.9478	0.0606
$\checkmark$	$\checkmark$	39.93	0.9484	0.0611

obtain better performance than the original 3-D convolution. When the rank upper bound exceeds  $3M$ , it only provides modest performance improvement. We thus adopt the ReS<sup>3</sup>-ConvSet with the rank upper bound of  $3M$ , i.e., Fig. 1(d), in all the remaining experiments.

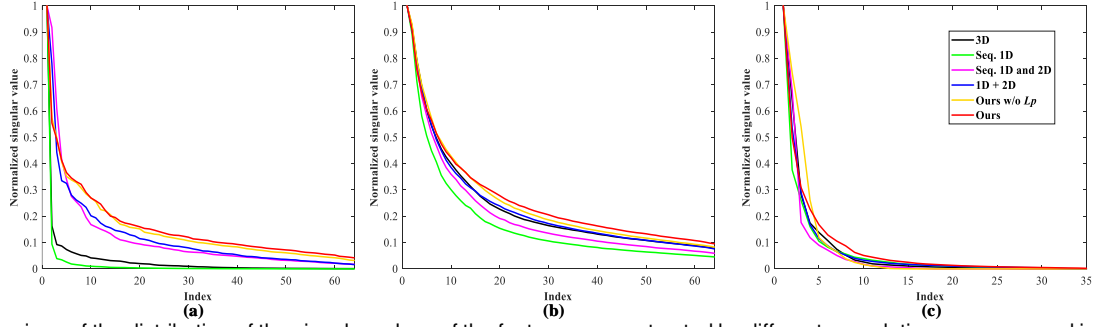


Fig. 12. Comparison of the distribution of the singular values of the feature maps extracted by different convolution manners used in the applications of (a) HS image denoising on the ICVL dataset with the Gaussian noise ( $\sigma = 70$ ), (b) HS image  $4\times$  spatial super-resolution on the CAVE dataset, and (c) HS image classification on Indian Pines. The singular values of each convolution scheme is normalized by its largest value.

TABLE 13

Results of the ablation study towards our ReS<sup>3</sup>-ConvSet and DA-Reg over HS image super-resolution with  $\alpha = 4$  on the CAVE dataset. For the first two settings, we replaced ReS<sup>3</sup>-ConvSet with 3-D convolution with an identical number of layers.

ReS <sup>3</sup> -ConvSet	DA-Reg	MPSNR $\uparrow$	MSSIM $\uparrow$	SAM $\downarrow$
$\times$	$\times$	40.98	0.9664	3.452
$\times$	$\checkmark$	41.08	0.9664	3.450
$\checkmark$	$\times$	41.35	0.9671	3.418
$\checkmark$	$\checkmark$	41.44	0.9672	3.412

TABLE 14

Results of the ablation study towards our rank loss over HS image classification on *Indian Pines*. For the first two settings, we replaced ReS<sup>3</sup>-ConvSet with 3-D convolution with an identical number of layers.

ReS <sup>3</sup> -ConvSet	DA-Reg	OA	AA	Kappa
$\times$	$\times$	82.38	90.37	0.8004
$\times$	$\checkmark$	83.66	90.36	0.8136
$\checkmark$	$\times$	85.32	91.86	0.8324
$\checkmark$	$\checkmark$	87.17	91.98	0.8524

#### 5.4.2 The number of ReS<sup>3</sup> blocks

We conducted ablation studies to explore how the number of ReS<sup>3</sup> blocks involved in our constructed denoising and super-resolution frameworks affects the performance.

For denoising, we varied the number of ReS<sup>3</sup> blocks in the range from 1 to 7. As shown in Fig. 11 (a), it can be observed that increasing the number of ReS<sup>3</sup> blocks is able to improve denoising performance. Observing that when the number of ReS<sup>3</sup> block goes up to 5, the denoising performance tends to be stable and even drops slightly, we hence set the number of ReS<sup>3</sup> blocks to 5 in all the remaining experiments of HS image denoising task.

For super-resolution, we evaluated with various numbers of ReS<sup>3</sup> blocks, i.e., 1, 4, 9, 11, and 13. As shown in Fig. 11 (b), it can be observed that with the number of ReS<sup>3</sup> blocks increasing, the quality of HS super-resolved image improves. However, when the number of ReS<sup>3</sup> block goes up to 11, the performance of our method starts to drop slightly, we thus chose the number of ReS<sup>3</sup> blocks to 11 in all the remaining experiments of HS image spatial super-resolution task.

#### 5.4.3 Contributions of ReS<sup>3</sup>-ConvSet and DA-Reg

Tables 12, 13, and 14 list the results of our constructed denoising, super-resolution, and classification frameworks with or without the proposed ReS<sup>3</sup>-ConvSet and DA-Reg. It

TABLE 15

Results of the ablation study towards the symmetry property of our ReS<sup>3</sup>-ConvSet over HS image denoising on the ICVL dataset with the Gaussian noise ( $\sigma = 70$ ). For the ReS<sup>3</sup>-ConvSet w/o symmetry, we utilized different numbers of channels for each 1-D convolution in ReS<sup>3</sup>-ConvSet, i.e., the three dimensions of the HS image are unequally essential in this setting.

Methods	MPSNR $\uparrow$	MSSIM $\uparrow$	SAM $\downarrow$
ReS <sup>3</sup> -ConvSet w/o symmetry	39.68	0.9471	0.0616
ReS <sup>3</sup> -ConvSet	39.85	0.9478	0.0606

TABLE 16

Results of the ablation study towards the symmetry property of our ReS<sup>3</sup>-ConvSet over HS image super-resolution with  $\alpha = 4$  on the CAVE dataset. For the ReS<sup>3</sup>-ConvSet w/o symmetry, we utilized different numbers of channels for each 1-D convolution in ReS<sup>3</sup>-ConvSet, i.e., the three dimensions of the HS image are unequally essential in this setting.

Methods	MPSNR $\uparrow$	MSSIM $\uparrow$	SAM $\downarrow$
ReS <sup>3</sup> -ConvSet w/o symmetry	41.20	0.9670	3.427
ReS <sup>3</sup> -ConvSet	41.35	0.9671	3.418

can be observed that both ReS<sup>3</sup>-ConvSet and DA-Reg make contributions to the satisfactory performance.

#### 5.4.4 Quantitative comparisons of various convolution manners

For fair comparisons, we built various denoising, super-resolution, and classification methods by only replacing the 1-D convolutional kernels in our ReS<sup>3</sup> block with the variants and retaining all the other settings (e.g., connections, aggregation, etc.). Besides, we also provided the results of 3-D convolution for reference. As listed in Tables 9, 10, and 11, it can be seen that compared with the 3-D convolution, all the convolution variants show their advantages on either quantitative performance or network compactness (#Params) and complexity (#FLOPs). Generally, a higher upper bound of the rank produces better performance, which is consistent with our theoretical analysis. Particularly, our ReS<sup>3</sup>-ConvSet equipped with the second fewest number of network parameters has the highest rank upper bound during the feature extraction process and thus achieves the best quantitative performance, convincingly demonstrating its superiority and the importance of filter diversity in designing feature extraction module.



#### 5.4.5 Distribution of singular values of the feature matrix

We compared the distributions of the singular values of the feature matrices learned by different convolution manners. Specifically, we unfolded the feature embeddings from different convolution patterns (i.e., 3-D, Sequential 1-D, Sequential 1-D and 2-D, 1-D + 2-D, and the proposed ReS<sup>3</sup>-ConvSet) into feature matrices. Then, we computed the singular values of these feature matrices via singular value decomposition (SVD). Note that we selected those feature embeddings from the layers at the same depth for a fair comparison. As shown in Fig. 12, it can be clearly seen that the singular values of the feature matrix by our methods decrease more slowly than those of other schemes, demonstrating that the proposed methods can avoid only a few large singular values dominating the feature space, thus promoting feature diversity.

#### 5.4.6 The symmetry property of our ReS<sup>3</sup>-ConvSet.

We validated the importance of symmetry property of our ReS<sup>3</sup>-ConvSet. As listed in Tables 15 and 16, it can be seen that our ReS<sup>3</sup>-ConvSet equipped with the symmetry property shows its advantage in reconstruction performance.

## 6 CONCLUSION

In this paper, we first proposed an efficient and effective feature embedding module, named ReS<sup>3</sup>-ConvSet, under the theoretical analysis that improving the rank of the matrix formed by unfolded convolutional filters can promote feature diversity. Specifically, originating from the altering the topology of 3-D convolution, ReS<sup>3</sup>-ConvSet promoted the rank upper-bound via separately performing 1-D convolution along the three dimensions of HS images side-by-side, thus making it not only well embed the high-dimensional spatio-spectral information of HS images but also reduce the computational complexity. In addition, we also designed a novel diversity-aware regularization term, named DA-Reg, to explicitly enhance feature diversity by regularizing the singular value distribution of unfolded feature volumes. We demonstrated the significant advantages of the proposed ReS<sup>3</sup>-ConvSet and DA-Reg by applying them to HS image denoising, spatial super-resolution, and classification.

## REFERENCES

- [1] M. Shimoni, R. Haelterman, and C. Perneel, "Hyperspectral imaging for military and security applications: Combining myriad processing and sensing techniques," *IEEE Geoscience and Remote Sensing Magazine*, vol. 7, no. 2, pp. 101–117, 2019.
- [2] B. Park and R. Lu, *Hyperspectral imaging technology in food and agriculture*. Springer, 2015.
- [3] Z. P. Lee, W. Rhea, R. Arnone, and W. Goode, "Absorption coefficients of marine waters: expanding multiband information to hyperspectral data," *IEEE Transactions on Geoscience and Remote Sensing*, vol. 43, no. 1, pp. 118–124, 2005.
- [4] Y. Chang, L. Yan, H. Fang, S. Zhong, and W. Liao, "Hsi-denet: Hyperspectral image restoration via convolutional neural network," *IEEE Transactions on Geoscience and Remote Sensing*, vol. 57, no. 2, pp. 667–682, 2019.
- [5] J. Jiang, H. Sun, X. Liu, and J. Ma, "Learning spatial-spectral prior for super-resolution of hyperspectral imagery," *IEEE Transactions on Computational Imaging*, vol. 6, pp. 1082–1096, 2020.
- [6] X. Cao, X. Fu, C. Xu, and D. Meng, "Deep spatial-spectral global reasoning network for hyperspectral image denoising," *IEEE Transactions on Geoscience and Remote Sensing*, pp. 1–14, 2021.
- [7] S. Mei, X. Yuan, J. Ji, Y. Zhang, S. Wan, and Q. Du, "Hyperspectral image spatial super-resolution via 3d full convolutional neural network," *Remote Sensing*, vol. 9, no. 11, p. 1139, 2017.
- [8] Q. Zhang, Q. Yuan, J. Li, X. Liu, H. Shen, and L. Zhang, "Hybrid noise removal in hyperspectral imagery with a spatial-spectral gradient network," *IEEE Transactions on Geoscience and Remote Sensing*, vol. 57, no. 10, pp. 7317–7329, 2019.
- [9] A. B. Hamida, A. Benoit, P. Lambert, and C. B. Amar, "3-d deep learning approach for remote sensing image classification," *IEEE Transactions on geoscience and remote sensing*, vol. 56, no. 8, pp. 4420–4434, 2018.
- [10] Q. Yuan, Q. Zhang, J. Li, H. Shen, and L. Zhang, "Hyperspectral image denoising employing a spatial-spectral deep residual convolutional neural network," *IEEE Transactions on Geoscience and Remote Sensing*, vol. 57, no. 2, pp. 1205–1218, 2019.
- [11] Q. Wang, Q. Li, and X. Li, "Hyperspectral image superresolution using spectrum and feature context," *IEEE Transactions on Industrial Electronics*, vol. 68, no. 11, pp. 11 276–11 285, 2021.
- [12] N. He, M. E. Paoletti, J. M. Haut, L. Fang, S. Li, A. Plaza, and J. Plaza, "Feature extraction with multiscale covariance maps for hyperspectral image classification," *IEEE Transactions on Geoscience and Remote Sensing*, vol. 57, no. 2, pp. 755–769, 2019.
- [13] Q. Shi, X. Tang, T. Yang, R. Liu, and L. Zhang, "Hyperspectral image denoising using a 3-d attention denoising network," *IEEE Transactions on Geoscience and Remote Sensing*, pp. 1–16, 2021.
- [14] X. Wang, K. Tan, P. Du, C. Pan, and J. Ding, "A unified multiscale learning framework for hyperspectral image classification," *IEEE Transactions on Geoscience and Remote Sensing*, vol. 60, pp. 1–19, 2022.
- [15] M. Zhu, L. Jiao, F. Liu, S. Yang, and J. Wang, "Residual spectral?spatial attention network for hyperspectral image classification," *IEEE Transactions on Geoscience and Remote Sensing*, vol. 59, no. 1, pp. 449–462, 2021.
- [16] M. E. Paoletti, S. Moreno-Álvarez, and J. M. Haut, "Multiple attention-guided capsule networks for hyperspectral image classification," *IEEE Transactions on Geoscience and Remote Sensing*, vol. 60, pp. 1–20, 2022.
- [17] W. Liu and J. Lee, "A 3-d atrous convolution neural network for hyperspectral image denoising," *IEEE Transactions on Geoscience and Remote Sensing*, vol. 57, no. 8, pp. 5701–5715, 2019.
- [18] M. Zhang, W. Li, and Q. Du, "Diverse region-based cnn for hyperspectral image classification," *IEEE Transactions on Image Processing*, vol. 27, no. 6, pp. 2623–2634, 2018.
- [19] F. Yang, X. Zhou, Y. Wang, A. Atawulla, and R. Bi, "Diversity features enhanced prototypical network for few-shot intent detection," in *Proc. International Joint Conference on Artificial Intelligence*, 7 2022, pp. 4447–4453.
- [20] P. Ghamisi, N. Yokoya, J. Li, W. Liao, S. Liu, J. Plaza, B. Rasti, and A. Plaza, "Advances in hyperspectral image and signal processing: A comprehensive overview of the state of the art," *IEEE Geoscience and Remote Sensing Magazine*, vol. 5, no. 4, pp. 37–78, 2017.
- [21] S. Li, W. Song, L. Fang, Y. Chen, P. Ghamisi, and J. A. Benediktsson, "Deep learning for hyperspectral image classification: An overview," *IEEE Transactions on Geoscience and Remote Sensing*, vol. 57, no. 9, pp. 6690–6709, 2019.
- [22] J. Peng, W. Sun, H.-C. Li, W. Li, X. Meng, C. Ge, and Q. Du, "Low-rank and sparse representation for hyperspectral image processing: A review," *IEEE Geoscience and Remote Sensing Magazine*, vol. 10, no. 1, pp. 10–43, 2022.
- [23] Z. Qiu, T. Yao, and T. Mei, "Learning spatio-temporal representation with pseudo-3d residual networks," in *Proc. IEEE/CVF International Conference on Computer Vision*, 2017, pp. 5534–5542.
- [24] W. Dong, H. Wang, F. Wu, G. Shi, and X. Li, "Deep spatial-spectral representation learning for hyperspectral image denoising," *IEEE Transactions on Computational Imaging*, vol. 5, no. 4, pp. 635–648, 2019.
- [25] K. Wei, Y. Fu, and H. Huang, "3-d quasi-recurrent neural network for hyperspectral image denoising," *IEEE Transactions on Neural Networks and Learning Systems*, vol. 32, no. 1, pp. 363–375, 2021.
- [26] H. Zhang, H. Chen, G. Yang, and L. Zhang, "Lr-net: Low-rank spatial-spectral network for hyperspectral image denoising," *IEEE Transactions on Image Processing*, vol. 30, pp. 8743–8758, 2021.
- [27] X. Rui, X. Cao, Q. Xie, Z. Yue, Q. Zhao, and D. Meng, "Learning an explicit weighting scheme for adapting complex hsi noise," in *Proc. IEEE/CVF Conference on Computer Vision and Pattern Recognition*, June 2021, pp. 6739–6748.

- [28] T. Bodrito, A. Zouaoui, J. Chanussot, and J. Mairal, "A trainable spectral-spatial sparse coding model for hyperspectral image restoration," in *Thirty-Fifth Conference on Neural Information Processing Systems*, 2021.
- [29] Y. Yuan, X. Zheng, and X. Lu, "Hyperspectral image super-resolution by transfer learning," *IEEE Journal of Selected Topics in Applied Earth Observations and Remote Sensing*, vol. 10, no. 5, pp. 1963–1974, 2017.
- [30] J. Li, R. Cui, B. Li, R. Song, Y. Li, Y. Dai, and Q. Du, "Hyperspectral image super-resolution by band attention through adversarial learning," *IEEE Transactions on Geoscience and Remote Sensing*, vol. 58, no. 6, pp. 4304–4318, 2020.
- [31] J. Hu, X. Jia, Y. Li, G. He, and M. Zhao, "Hyperspectral image super-resolution via intrafusion network," *IEEE Transactions on Geoscience and Remote Sensing*, vol. 58, no. 10, pp. 7459–7471, 2020.
- [32] Q. Li, Q. Wang, and X. Li, "Exploring the relationship between 2d/3d convolution for hyperspectral image super-resolution," *IEEE Transactions on Geoscience and Remote Sensing*, pp. 1–11, 2021.
- [33] K. Li, D. Dai, and L. Van Gool, "Hyperspectral image super-resolution with rgb image super-resolution as an auxiliary task," in *Proc. IEEE/CVF Winter Conference on Applications of Computer Vision (WACV)*, 2022, pp. 4039–4048.
- [34] X. Wang, J. Ma, and J. Jiang, "Hyperspectral image super-resolution via recurrent feedback embedding and spatial/spectral consistency regularization," *IEEE Transactions on Geoscience and Remote Sensing*, vol. 60, pp. 1–13, 2022.
- [35] J. Hou, Z. Zhu, J. Hou, H. Zeng, J. Wu, and J. Zhou, "Deep posterior distribution-based embedding for hyperspectral image super-resolution," *IEEE Transactions on Image Processing*, vol. 31, pp. 5720–5732, 2022.
- [36] F. Melgani and L. Bruzzone, "Classification of hyperspectral remote sensing images with support vector machines," *IEEE Transactions on geoscience and remote sensing*, vol. 42, no. 8, pp. 1778–1790, 2004.
- [37] J. Ham, Y. Chen, M. M. Crawford, and J. Ghosh, "Investigation of the random forest framework for classification of hyperspectral data," *IEEE Transactions on Geoscience and Remote Sensing*, vol. 43, no. 3, pp. 492–501, 2005.
- [38] Y. Bazi and F. Melgani, "Gaussian process approach to remote sensing image classification," *IEEE transactions on geoscience and remote sensing*, vol. 48, no. 1, pp. 186–197, 2009.
- [39] L. Ma, M. M. Crawford, and J. Tian, "Local manifold learning-based  $k$ -nearest-neighbor for hyperspectral image classification," *IEEE Transactions on Geoscience and Remote Sensing*, vol. 48, no. 11, pp. 4099–4109, 2010.
- [40] T. V. Bandos, L. Bruzzone, and G. Camps-Valls, "Classification of hyperspectral images with regularized linear discriminant analysis," *IEEE Transactions on Geoscience and Remote Sensing*, vol. 47, no. 3, pp. 862–873, 2009.
- [41] G. Licciardi, P. R. Marpu, J. Chanussot, and J. A. Benediktsson, "Linear versus nonlinear pca for the classification of hyperspectral data based on the extended morphological profiles," *IEEE Geoscience and Remote Sensing Letters*, vol. 9, no. 3, pp. 447–451, 2012.
- [42] Y. Chen, Z. Lin, X. Zhao, G. Wang, and Y. Gu, "Deep learning-based classification of hyperspectral data," *IEEE Journal of Selected topics in applied earth observations and remote sensing*, vol. 7, no. 6, pp. 2094–2107, 2014.
- [43] W. Hu, Y. Huang, L. Wei, F. Zhang, and H. Li, "Deep convolutional neural networks for hyperspectral image classification," *Journal of Sensors*, vol. 2015, 2015.
- [44] Y. Chen, H. Jiang, C. Li, X. Jia, and P. Ghamisi, "Deep feature extraction and classification of hyperspectral images based on convolutional neural networks," *IEEE Transactions on Geoscience and Remote Sensing*, vol. 54, no. 10, pp. 6232–6251, 2016.
- [45] M. E. Paoletti, J. M. Haut, R. Fernandez-Beltran, J. Plaza, A. J. Plaza, and F. Pla, "Deep pyramidal residual networks for spectral-spatial hyperspectral image classification," *IEEE Transactions on Geoscience and Remote Sensing*, vol. 57, no. 2, pp. 740–754, 2019.
- [46] L. Mou, P. Ghamisi, and X. X. Zhu, "Deep recurrent neural networks for hyperspectral image classification," *IEEE Transactions on Geoscience and Remote Sensing*, vol. 55, no. 7, pp. 3639–3655, 2017.
- [47] D. Hong, L. Gao, J. Yao, B. Zhang, A. Plaza, and J. Chanussot, "Graph convolutional networks for hyperspectral image classification," *IEEE Transactions on Geoscience and Remote Sensing*, vol. 59, no. 7, pp. 5966–5978, 2021.
- [48] R. Hang, F. Zhou, Q. Liu, and P. Ghamisi, "Classification of hyperspectral images via multitask generative adversarial networks," *IEEE Transactions on Geoscience and Remote Sensing*, vol. 59, no. 2, pp. 1424–1436, 2021.
- [49] D. Hong, Z. Han, J. Yao, L. Gao, B. Zhang, A. Plaza, and J. Chanussot, "Spectralformer: Rethinking hyperspectral image classification with transformers," *IEEE Transactions on Geoscience and Remote Sensing*, vol. 60, pp. 1–15, 2022.
- [50] Y. Chen, X. Jin, J. Feng, and S. Yan, "Training group orthogonal neural networks with privileged information," in *Proc. International Joint Conference on Artificial Intelligence (IJCAI)*, 2017.
- [51] J. Wang, Y. Chen, R. Chakraborty, and S. X. Yu, "Orthogonal convolutional neural networks," in *Proc. IEEE/CVF conference on computer vision and pattern recognition*, 2020, pp. 11 505–11 515.
- [52] F. Heide, W. Heidrich, and G. Wetzstein, "Fast and flexible convolutional sparse coding," in *Proc. IEEE/CVF Conference on Computer Vision and Pattern Recognition*, 2015, pp. 5135–5143.
- [53] K. Yanai, R. Tanno, and K. Okamoto, "Efficient mobile implementation of a cnn-based object recognition system," in *Proc. 24th ACM international conference on Multimedia*, 2016, pp. 362–366.
- [54] M. Denil, B. Shakibi, L. Dinh, M. Ranzato, and N. De Freitas, "Predicting parameters in deep learning," *Advances in neural information processing systems*, vol. 26, 2013.
- [55] W. Shang, K. Sohn, D. Almeida, and H. Lee, "Understanding and improving convolutional neural networks via concatenated rectified linear units," in *Proc. international conference on machine learning*. PMLR, 2016, pp. 2217–2225.
- [56] M. Lin, R. Ji, Y. Wang, Y. Zhang, B. Zhang, Y. Tian, and L. Shao, "Hrank: Filter pruning using high-rank feature map," in *Proc. IEEE/CVF Conference on Computer Vision and Pattern Recognition*, 2020, pp. 1526–1535.
- [57] L. Zhang, Q. Zhang, B. Du, X. Huang, Y. Y. Tang, and D. Tao, "Simultaneous spectral-spatial feature selection and extraction for hyperspectral images," *IEEE Transactions on Cybernetics*, vol. 48, no. 1, pp. 16–28, 2016.
- [58] O. Ronneberger, P. Fischer, and T. Brox, "U-net: Convolutional networks for biomedical image segmentation," in *International Conference on Medical image computing and computer-assisted intervention*. Springer, 2015, pp. 234–241.
- [59] Y. Zhang, Y. Tian, Y. Kong, B. Zhong, and Y. Fu, "Residual dense network for image super-resolution," in *Proc. IEEE conference on computer vision and pattern recognition*, 2018, pp. 2472–2481.
- [60] H. Zhang, W. He, L. Zhang, H. Shen, and Q. Yuan, "Hyperspectral image restoration using low-rank matrix recovery," *IEEE Transactions on Geoscience and Remote Sensing*, vol. 52, no. 8, pp. 4729–4743, 2014.
- [61] Y. Chen, X. Cao, Q. Zhao, D. Meng, and Z. Xu, "Denoising hyperspectral image with non-i.i.d. noise structure," *IEEE Transactions on Cybernetics*, vol. 48, no. 3, pp. 1054–1066, 2018.
- [62] Y. Wang, J. Peng, Q. Zhao, Y. Leung, X.-L. Zhao, and D. Meng, "Hyperspectral image restoration via total variation regularized low-rank tensor decomposition," *IEEE Journal of Selected Topics in Applied Earth Observations and Remote Sensing*, vol. 11, no. 4, pp. 1227–1243, 2018.
- [63] Q. Xie, Q. Zhao, D. Meng, Z. Xu, S. Gu, W. Zuo, and L. Zhang, "Multispectral images denoising by intrinsic tensor sparsity regularization," in *Proc. IEEE/CVF Conference on Computer Vision and Pattern Recognition*, 2016, pp. 1692–1700.
- [64] W. He, Q. Yao, C. Li, N. Yokoya, Q. Zhao, H. Zhang, and L. Zhang, "Non-local meets global: An iterative paradigm for hyperspectral image restoration," *IEEE Transactions on Pattern Analysis and Machine Intelligence*, vol. 44, no. 4, pp. 2089–2107, 2022.
- [65] B. Arad and O. Ben-Shahar, "Sparse recovery of hyperspectral signal from natural rgb images," in *Proc. European Conference on Computer Vision*. Springer, 2016, pp. 19–34.
- [66] D. P. Kingma and J. Ba, "Adam: A method for stochastic optimization," *arXiv preprint arXiv:1412.6980*, 2014.
- [67] J. Jiang, D. Liu, J. Gu, and S. Süsstrunk, "What is the space of spectral sensitivity functions for digital color cameras?" in *Proc. IEEE Workshop on Applications of Computer Vision*. IEEE, 2013, pp. 168–179.
- [68] Z. Wang, A. C. Bovik, H. R. Sheikh, and E. P. Simoncelli, "Image quality assessment: from error visibility to structural similarity," *IEEE transactions on image processing*, vol. 13, no. 4, pp. 600–612, 2004.
- [69] R. H. Yuhas, A. F. Goetz, and J. W. Boardman, "Discrimination among semi-arid landscape endmembers using the spectral angle

- mapper (sam) algorithm," in *Proc. Summaries 3rd Annu. JPL Airborne Geosci. Workshop*, vol. 1, 1992, pp. 147–149.
- [70] F. Yasuma, T. Mitsunaga, D. Iso, and S. K. Nayar, "Generalized assorted pixel camera: Postcapture control of resolution, dynamic range, and spectrum," *IEEE Transactions on Image Processing*, vol. 19, no. 9, pp. 2241–2253, 2010.
- [71] A. Vaswani, N. Shazeer, N. Parmar, J. Uszkoreit, L. Jones, A. N. Gomez, Ł. Kaiser, and I. Polosukhin, "Attention is all you need," *Advances in neural information processing systems*, vol. 30, 2017.